

Resonant inelastic x-ray scattering in a Mott insulatorNandan Pakhira,¹ J. K. Freericks,¹ and A. M. Shvaika²¹*Department of Physics, Georgetown University, Washington, DC 20057, USA*²*Institute for Condensed Matter Physics of the National Academy of Sciences of Ukraine, 1 Svientsitskii Street, 79011 Lviv, Ukraine*

(Received 20 December 2011; published 5 September 2012)

We calculate the resonant inelastic x-ray scattering (RIXS) response in a Mott insulator, which is described by the Falicov-Kimball model. The model can be solved exactly within the single site dynamical mean-field theory (DMFT) approximation and the RIXS response can also be calculated accurately up to a local background correction. We find that on resonance the RIXS response is greatly enhanced. The response systematically evolves from a single-peak structure, arising due to relaxation processes within the lower Hubbard band, to a two-peak structure, arising due to relaxation processes within the upper Hubbard band and across the Mott gap into the lower Hubbard band. This occurs as we vary the incident photon frequency to allow excitations from the lower Hubbard band to the upper Hubbard band. The charge transfer excitations are found to disperse monotonically as we go from the center of the Brillouin zone towards the zone corner. These correlation-induced features have been observed by Hasan *et al.* [*Science* **288**, 1811 (2000)] and many other experimentalists in RIXS measurements over various transition-metal oxide compounds. They are found to be robust and survive even for large Auger lifetime broadening effects that can mask the many-body effects by smearing out spectral features. As a comparison, we also calculate the dynamic structure factor for this model, which is proportional to the nonresonant part of the response, and does not show these specific signatures.

DOI: [10.1103/PhysRevB.86.125103](https://doi.org/10.1103/PhysRevB.86.125103)

PACS number(s): 71.10.Fd, 71.27.+a, 74.72.-h, 78.70.Ck

I. INTRODUCTION

Resonant inelastic x-ray scattering is essentially a deep core level spectroscopic method that is increasingly becoming an essential technique in understanding the complex electronic dynamics of a wide class of novel materials like cuprates, manganites, and various other transition-metal oxide compounds. In the RIXS process, a highly energetic x-ray photon (with energy $\sim 1-10$ keV) excites a deep core level electron into the unoccupied states of the conduction band. The excited electron then undergoes inelastic scattering processes with various intrinsic excitations present in the system and finally, a conduction band electron fills up the core-hole and emits a photon with relatively lower energy. So, this is a two-photon inelastic process with no core-hole present in the final state. The transferred energy and momentum to the intrinsic excitations of the system as well as the change in the polarization of the scattered photon can provide important information regarding these excitations. Also, RIXS being a resonant technique, the incident photon energy can be chosen to coincide with, and hence resonate with, certain intrinsic x-ray atomic transitions which in effect can greatly enhance the inelastic scattering cross section. This enhancement allows RIXS to be used as a probe for charge, magnetic, and orbital degrees of freedom on selective atomic sites.

RIXS has several advantages over other spectroscopic techniques like angle resolved photo-emission spectroscopy (ARPES) and neutron scattering. First, in ARPES, the incident photon knocks out an electron from the system and hence can only probe the occupied states in a system, whereas RIXS, being a high-energy process, can excite a system into unoccupied intermediate states (like the upper Hubbard band in a Mott insulator) and hence can be used as a probe for understanding complex electron dynamics in those strongly correlated intermediate states. Inverse photoemission techniques, in which an electron is injected into the system,

can also access the unoccupied states of a system. But this method will charge the system and so far no momentum resolved inverse photoemission spectroscopy with sufficient energy resolution has been developed. Second, the scattering phase space, i.e., the range of energies and momenta that can be transferred in the RIXS process, is much larger than other available photon scattering techniques involving visible or infrared light. As a result, RIXS can probe low-energy excitations over a wider range of the Brillouin zone and most importantly it can be used to probe all three directions of the Brillouin zone, and hence can be used even for materials that are intrinsically three dimensional in nature. On the other hand, ARPES, because of the in plane momentum conservation, is widely used for materials which are inherently two dimensional in nature. For three-dimensional materials, the analysis of ARPES spectra is much more complicated (the perpendicular component of momentum is integrated over in the ARPES spectra). Another advantage is that the electron-photon interaction is much stronger than the electron-neutron interaction (which arises through the magnetic dipole-dipole interaction). As a result, RIXS can be used on small volume samples, thin films, surfaces, and nano-objects in addition to bulk single crystal or powder samples. Besides these, RIXS is polarization dependent and hence can be used to probe magnetic excitations and also it can be used as a probe for certain specific elements or orbitals in a system. The main disadvantage of RIXS over other techniques is that it requires substantially large incident photon flux in order to have comparable or better energy and momentum resolution. But recent progress in RIXS instrumentation has dramatically improved upon this situation and RIXS is beginning to become an important probe for condensed matter physics.

Over the past decade or so, RIXS measurements have been performed over large classes of transition-metal oxide compounds like cuprates, manganites, iridates, etc. (see Ref. 1 for a detailed review). Most notably, RIXS

measurements have been performed at the Cu K edge^{2–11} over a large class of cuprates like the undoped La_2CuO_4 ,^{3,7} Nd_2CuO_4 ,^{2,4} $\text{Sr}_2\text{CuO}_2\text{Cl}_2$,² $\text{Ca}_2\text{CuO}_2\text{Cl}_2$,⁵ quasi-one-dimensional cuprates like SrCuO_2 ,^{6,8} Sr_2CuO_3 ,⁶ hole-doped cuprates $\text{La}_{2-x}\text{Sr}_x\text{CuO}_4$,¹¹ $\text{YBa}_2\text{Cu}_3\text{O}_{7-\delta}$,⁹ and electron-doped cuprates $\text{Nd}_{1.85}\text{Ce}_{0.15}\text{CuO}_4$.¹⁰ Also, RIXS has been performed at the Cu L_3 edge^{12–14} over various undoped cuprates CuO ,¹² $\text{Sr}_2\text{CuO}_2\text{Cl}_2$,¹² La_2CuO_4 ,^{12,14} and doped systems $\text{Bi}_2\text{Sr}_2\text{CaCu}_2\text{O}_{8+\delta}$, $\text{Nd}_{2-x}\text{Ce}_x\text{CuO}_4$,¹² $\text{La}_{2-x}\text{Sr}_x\text{CuO}_4$.^{12–14} Besides these, RIXS measurements at the Mn K edge in the orbitally ordered manganite LaMnO_3 ,¹⁵ at the Mn $L_{2,3}$ absorption edge in MnO ,¹⁶ at the Ni L_3 -edge in NiO ,¹⁷ and at the Ir L_3 edge in the $5d$ Mott insulator Sr_2IrO_4 ^{18,19} have also been reported. A common feature of these materials is that all of them are either Mott insulators or doped Mott insulators and have interesting magnetic ground states. RIXS measurements on these materials have probed energy and momentum resolved features of charge transfer excitations,^{5,6,19} dd excitations^{12,13,16} (arising due to transitions between crystal field split d orbitals), orbitons¹⁵ in orbitally ordered systems and even magnetic excitations like magnons¹⁴ and bimagnons.¹¹

Theoretical approaches in understanding the RIXS response are mainly either based on exact diagonalization of model Hamiltonians over finite but small clusters^{5,20–23} (typically with a large Auger broadening put in by hand) or based on a single-particle approach^{24–30} that includes realistic band structure effects. The correlation effects are treated perturbatively under the random phase approximation^{24–28} (RPA) or under a self-consistent renormalization^{29,30} (SCR) approach and the effect of scattering from the core hole in the first-order Born approximation or multiple scattering approximation. The exact diagonalization method treats the strong correlation effects exactly but because of the exponentially growing basis problem, this method is limited to small size clusters and small number of orbitals and hence has limited momentum resolution. Also, the effects of the core hole in this approach as well as in the SCR-based calculations are taken either through an input core-hole lifetime, arising due to Auger and fluorescence effects, which broadens the intermediate states or under the ultrashort core-hole lifetime (UCL) approximation^{31,32} that is found to be perturbatively exact for small as well as large core-hole potentials. But the effect of the core-hole lifetime arising solely due to intrinsic strong correlation effects in a Mott insulator on the RIXS response has not been addressed so far and in this work we use the Falicov-Kimball³³ (FK) model to address this issue. The main motivation in choosing the FK model is that the FK model is one of the simplest models of strongly correlated electron systems that can be exactly solved^{34,35} under the single-site dynamical mean-field theory^{36,37} (DMFT) approximation and most notably shows a Mott insulating ground state for large interaction strength between the itinerant and the static electrons. Also, the fully renormalized two-particle dynamic charge correlation function involving the itinerant species as well as the finite temperature core-hole propagator in this model can be calculated exactly.

One might ask how this solution for RIXS in the Falicov-Kimball model compares with the solution in the Hubbard model. Since the exact solution for the Hubbard model is not known, we can only speculate here. But because the

predominant property of the Mott phase (above the magnetic ordering temperature) is its gap, we expect that much of the results in this regime will be generic to the two models. This reasoning has shown to be true when comparing Raman scattering calculated in the Falicov-Kimball model to that calculated in the Hubbard model,^{38,39} where in the insulating phase much of the behavior was quite similar, with details varying in the temperature dependence.

In the following sections, we calculate the RIXS response in the limit of large core-hole energy using only two approximations: (1) we neglect some momentum independent background contributions and (2) we calculate the charge vertex for the core-hole–band-electron exchange processes (see below) under the Hartree-Fock approximation. The organization of the paper is as follows. In Sec. II, we provide a brief mathematical formulation for the calculation of the RIXS cross section followed by Sec. III where we show a more detailed calculation for the RIXS response in the FK model. In Sec. IV, we show our results for a half-filled Mott insulator followed by Sec. V where we discuss the core-hole lifetime broadening effects on the RIXS response and in Sec. VI we show some results for the case of particle-hole asymmetric Mott insulator. Finally, in Sec. VII we conclude.

II. MATHEMATICAL FORMULATION OF RIXS

Our starting point is the familiar electron-photon interaction Hamiltonian¹

$$H_{\text{int}} = \sum_{i=1}^N \left[\frac{e}{m} \mathbf{A}(\mathbf{r}_i, t) \cdot \mathbf{p}_i + \frac{e\hbar}{2m} \boldsymbol{\sigma}_i \cdot \nabla \times \mathbf{A}(\mathbf{r}_i, t) + \frac{e^2}{2m} \mathbf{A}^2(\mathbf{r}_i, t) - \frac{e^2\hbar}{4m^2c^2} \boldsymbol{\sigma}_i \cdot \frac{\partial \mathbf{A}(\mathbf{r}_i, t)}{\partial t} \times \mathbf{A}(\mathbf{r}_i, t) \right] \quad (1)$$

for a system of N electrons. $\mathbf{A}(\mathbf{r}, t)$ is the vector potential for the external electromagnetic field and can be expanded in a plane-wave basis as

$$\mathbf{A}(\mathbf{r}, t) = \sum_{\mathbf{k}, \varepsilon} \sqrt{A_0} [\boldsymbol{\varepsilon} a_{\mathbf{k}\varepsilon} e^{i(\mathbf{k}\cdot\mathbf{r}-\omega t)} + \boldsymbol{\varepsilon}^* a_{-\mathbf{k}\varepsilon}^\dagger e^{-i(\mathbf{k}\cdot\mathbf{r}-\omega t)}], \quad (2)$$

where $A_0 = \frac{\hbar}{2V\varepsilon_0\omega\mathbf{k}}$, V is the volume of the system, and $\boldsymbol{\varepsilon}$ is the polarization of the light, and we have fixed the gauge by choosing $\nabla \cdot \mathbf{A}(\mathbf{r}, t) = 0$ in Eq. (1).

In the RIXS process, an incident x-ray photon with momentum \mathbf{k}_i , energy ω_i , and polarization $\boldsymbol{\varepsilon}_i$ is scattered to a final state described by momentum \mathbf{k}_f , energy ω_f , and polarization $\boldsymbol{\varepsilon}_f$. Fermi's golden rule to second order in H_{int} gives the scattering cross section for this process:

$$\mathcal{W} = \frac{2\pi}{\hbar} \sum_{\mathbf{F}, \mathbf{I}} \left| \langle \mathbf{F} | H_{\text{int}} | \mathbf{I} \rangle + \sum_n \frac{\langle \mathbf{F} | H_{\text{int}} | n \rangle \langle n | H_{\text{int}} | \mathbf{I} \rangle}{E_{\mathbf{I}} - \epsilon_n} \right|^2 \times \rho(\boldsymbol{\varepsilon}_i) \delta(E_{\mathbf{F}} - E_{\mathbf{I}}), \quad (3)$$

where $|\mathbf{I}\rangle \equiv |i\rangle \otimes |\mathbf{k}_i, \omega_i\rangle$, $|\mathbf{F}\rangle \equiv |f\rangle \otimes |\mathbf{k}_f, \omega_f\rangle$, and $|n\rangle$ are the direct product states for the initial, final and the intermediate states of the systems, respectively (both electronic and photon states are present in the initial and final states, while the intermediate states are just the electronic states), and $E_{\mathbf{I}}$, $E_{\mathbf{F}}$, and ϵ_n are the corresponding energies, respectively. It

is interesting to mention that the intermediate state $|n\rangle$ has a core hole, while the initial and final states, $|\mathbf{I}\rangle$ and $|\mathbf{F}\rangle$, have no core hole. Also, at finite temperature, the system is in a *mixed state*, so we sum over all possible initial configurations weighted by the appropriate Boltzman factor, $\rho(\epsilon_i)$. The first-order amplitude is in general dominant over the second-order contribution except near resonance when the incident photon energy is nearly equal to a specific atomic transition in a material, i.e., $\omega_i \approx \epsilon_n - \epsilon_i$. At resonance, the second-order term becomes overwhelmingly large compared to the first-order term and hence the second-order term causes resonant scattering while the first-order term gives rise to nonresonant scattering.

The diamagnetic term proportional to \mathbf{A}^2 as well as the spin-orbit coupling term proportional to $\boldsymbol{\sigma} \cdot (\partial\mathbf{A}/\partial t) \times \mathbf{A}$ in Eq. (1) contribute to the first-order amplitude. The latter is smaller than the former by a factor of $\omega_{i(f)}/mc^2 \ll 1$ and also, at resonance, the contribution from the diamagnetic term is negligibly small compared to the resonant term and hence their contributions will be neglected. So, then the resonant part of the second-order amplitude at zero temperature is given by^{1,40,41}

$$\frac{e^2 \hbar \sqrt{\omega_{\mathbf{k}_i} \omega_{\mathbf{k}_f}}}{\mathcal{V} \epsilon_0} \sum_n \left[\frac{\langle f | \mathcal{D}_{\mathbf{k}_f} | n \rangle \langle n | \mathcal{D}_{-\mathbf{k}_i}^\dagger | i \rangle}{\epsilon_n - \epsilon_i - \omega_i} + \frac{\langle f | \mathcal{D}_{-\mathbf{k}_i}^\dagger | n \rangle \langle n | \mathcal{D}_{\mathbf{k}_f} | i \rangle}{\epsilon_n - \epsilon_i + \omega_f} \right], \quad (4)$$

where

$$\mathcal{D}_{\mathbf{k}} = \frac{1}{im\omega_{\mathbf{k}}} \sum_{i=1}^N e^{i\mathbf{k} \cdot \mathbf{r}_i} \left(\boldsymbol{\epsilon} \cdot \mathbf{p}_i + \frac{i\hbar}{2} \boldsymbol{\sigma}_i \cdot \mathbf{k} \times \boldsymbol{\epsilon} \right) \quad (5)$$

is the relevant transition operator for the RIXS cross section. The first term in Eq. (5) causes nonmagnetic scattering. The second term, arising from the spin-orbit coupling term in H_{int} , causes magnetic scattering which, for typical incident photon energy ($\sim 1-10$ keV) and the localized core levels involved in a RIXS process, is about 100 times smaller than the non-magnetic term¹ and hence will also be neglected. Finally, under such circumstances, we assume the dipole limit for the RIXS process and the transition operator is then given by

$$\mathcal{D} = \boldsymbol{\epsilon} \cdot \mathbf{D} \quad \text{with} \quad \mathbf{D} = \frac{1}{im\omega_{\mathbf{k}}} \sum_{i=1}^N \mathbf{p}_i. \quad (6)$$

The expression for the transition operator is model specific, and in the following section, we will explicitly show it for the Falicov-Kimball model.

III. RIXS RESPONSE IN THE FALICOV-KIMBALL MODEL

The Falicov-Kimball³³ model involves the interaction of mobile conduction electrons with static localized electrons. It was originally developed for rare-earth compounds, and hence the particles were denoted as d electrons for the conduction electrons and f electrons for the localized electrons. One can apply it in an approximate way to transition metal compounds where the labels d and f should no longer be associated with the corresponding atomic orbitals. The Hamiltonian for the

Falicov-Kimball model (in the hole representation) including the interaction with a core hole is given by

$$\begin{aligned} H = & -\frac{t^*}{2\sqrt{d}} \sum_{\langle ij \rangle} d_i^\dagger d_j - \sum_i \mu n_{di} + \sum_i (E_f - \mu) n_{fi} \\ & + \sum_i (E_h - \mu) n_{hi} + \sum_i U n_{di} n_{fi} + \sum_i Q_d n_{di} n_{hi} \\ & + \sum_i Q_f n_{fi} n_{hi}, \end{aligned} \quad (7)$$

where $n_{di} = d_i^\dagger d_i$, $n_{fi} = f_i^\dagger f_i$, and $n_{hi} = h_i^\dagger h_i$ are the occupation number operators for the d -hole, f -hole, and core-hole state at a given site i , respectively. $t^*/2\sqrt{d}$ is the nearest-neighbor hopping amplitude of the itinerant d hole on a d -dimensional hypercubic lattice and μ is the common chemical potential. U is the onsite Coulomb interaction between the itinerant d and the static f holes, $Q_d > 0$ and $Q_f > 0$ are the Coulomb interactions between the core hole, the d and f holes, respectively, E_f is the site energy of the f state and $E_h \sim 10^2-10^4$ eV is the energy of the core-hole state. It is important to mention that at half-filling ($\langle n_f \rangle = \langle n_d \rangle = 0.5$), we choose $\mu = U/2$ and $E_f = 0$, which corresponds to the particle-hole symmetric case (in the restricted subspace involving d and f operators). It is important to mention that under the hole-particle transformation $d \rightarrow d^\dagger$, $f \rightarrow f^\dagger$ the interactions between core-hole and band states transform as $Q_d \rightarrow -Q_d$, $Q_f \rightarrow -Q_f$, i.e., they become attractive instead of repulsive and the core-hole energy, E_h gets shifted to $E_h + Q_d + Q_f$.

Under single-site DMFT the model reduces to an effective single impurity problem,^{34,35} described by the local Hamiltonian

$$\begin{aligned} H_{\text{loc}} = & U n_d n_f + Q_d n_d n_h + Q_f n_f n_h - \mu n_d \\ & + (E_f - \mu) n_f + (E_h - \mu) n_h \end{aligned} \quad (8)$$

together with an *effective bath* to which the d holes hop in and out. The equilibrium density matrix for the single-impurity problem in DMFT is then given by

$$\rho = \frac{e^{-\beta H_{\text{loc}}}}{\mathcal{Z}} \mathcal{T}_c \exp \left[-i \int_c dt' \int_c dt'' d^\dagger(t') \lambda(t', t'') d(t'') \right], \quad (9)$$

where the time ordering and integration are performed over the Kadanoff-Baym-Keldysh contour (see Fig. 1) and $\beta = 1/k_B T$ is the inverse temperature. Here, the dynamical mean field $\lambda_c(t', t'')$ and the chemical potential μ are taken from the equilibrium solution of the conduction electron problem without the core hole, arising under the single-site DMFT approximation. This in effect implies that we are treating the creation of the core hole under the sudden approximation instead of a full nonequilibrium treatment of the core-hole propagator.

The equilibrium *impurity problem* arising under the DMFT approximation can be solved *exactly* in this case and the *local* d -hole propagator, $G_d^{\text{loc}}(\omega)$, is given by

$$G_d^{\text{loc}}(\omega) = \frac{w_0}{\omega^\pm + \mu - \lambda(\omega^\pm)} + \frac{w_1}{\omega^\pm + \mu - \lambda(\omega^\pm) - U}, \quad (10)$$

where $\omega^\pm = \omega \pm i\delta$ ($\delta > 0$) and w_0 and w_1 are the probabilities for finding a given site unoccupied and occupied

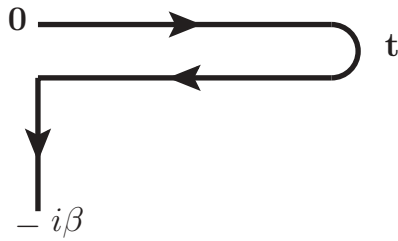


FIG. 1. The Kadanoff-Baym-Keldysh contour. The contour starts at time zero, moves forward along the real axis to time t then moves backward along the real axis to time zero, and finally, downwards along the imaginary axis to time $-i\beta$.

by an f hole, respectively. The momentum-dependent fully renormalized d -hole propagator is given by

$$G_d(\mathbf{q}, \omega) = \frac{1}{\omega^+ + \mu - \epsilon_{\mathbf{q}} - \Sigma_d^{\text{loc}}(\omega^+)}, \quad (11)$$

where the *local* self-energy is related to the *local* propagator through Dyson's equation

$$\Sigma_d^{\text{loc}}(\omega^+) = \omega^+ + \mu - \lambda(\omega^+) - [G_d^{\text{loc}}(\omega^+)]^{-1}. \quad (12)$$

Similarly, the core-hole Green's functions, $G_h^>(t) = -i \langle h(t)h^\dagger(0) \rangle$ and $G_h^<(t) = i \langle h^\dagger(0)h(t) \rangle$, can also be calculated⁴² at finite temperature by using either numerical integration over the Kadanoff-Baym-Keldysh contour as shown in Fig. 1 or by the Wiener-Hopf sum equation approach.^{43,44} The angular brackets $\langle \rangle$ denote a trace over all states weighted by density matrix in Eq. (9) and the operators are in the interaction representation with respect to H_{loc} . Also, it is important to mention that for the calculation of the itinerant as well as the core-hole propagators we use the d -dimensional hypercubic lattice density of states (DOS) in the limit of $d \rightarrow \infty$ (DMFT approximation).

The interaction of the x-ray photon with the electronic subsystem of matter can be represented by the diagrams shown in Fig. 2. The dipole operator^{31,32} is given by

$$D = \sum_l (e^{-i\mathbf{k}_i \cdot \mathbf{r}_l} h_l^\dagger d_l + e^{i\mathbf{k}_f \cdot \mathbf{r}_l} h_l d_l^\dagger + \text{H.c.}). \quad (13)$$

The first two terms in Eq. (13) correspond to Figs. 2(a) and 2(b), while the Hermitian conjugate terms correspond to Figs. 2(c) and 2(d). We have explicitly shown the direct dependence of the core-hole propagator on the core-hole energy E_h , which is typically much larger than the band energies and is of the order of the incident (ω_i) and the scattered (ω_f) x-ray photon energies, respectively. One can see that in the case of large photon and core-hole energies only the first two vertices [see Figs. 2(a) and 2(b)] contribute significantly whereas the contribution from the remaining two [see Figs. 2(c) and 2(d)] are negligibly small because the hole propagators are evaluated too far off the energy shell.

The calculation of the RIXS cross section involves the analytic continuation of the four-particle correlation function

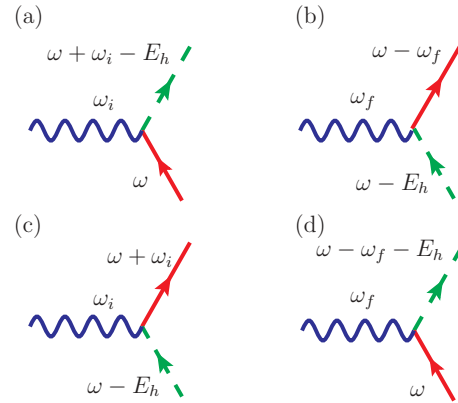


FIG. 2. (Color online) RIXS interaction vertices. Wavy lines (blue) represent incident or scattered photons, the dashed lines (green) represent the core-hole propagator, and the solid lines (red) represent the propagator for the itinerant d holes. The labels indicate the energies of the different particles. Note that the momentum and energy are conserved at each vertex.

$\chi_{i,f,f,i}^{(4)}(i\nu_i, i\nu_f, i\nu'_f, i\nu'_i)$ from Matsubara frequencies

$$\chi_{i,f,f,i}^{(4)}(i\nu_i, i\nu_f, i\nu'_f, i\nu'_i) \xrightarrow{F.T.} \chi^{(4)}(\tau_1, \tau_2, \tau_3, \tau_4) \quad (14)$$

$$\chi^{(4)}(\tau_1, \tau_2, \tau_3, \tau_4) = -\langle T_\tau D(\tau_1)D(\tau_2)D(\tau_3)D(\tau_4) \rangle$$

to real frequencies, which is a well defined but tedious procedure.^{45,46} In the considered limit of large photon and core-hole energies, the bare-loop contribution to the amplitude for the RIXS process is represented by the two diagrams shown in Fig. 3. The contribution of the top diagram to the four-particle correlation function, $\chi_{i,f,f,i}^{(4)}(i\nu_i, i\nu_f, i\nu'_f, i\nu'_i)$, evaluated on the imaginary axis, is equal to

$$-\frac{1}{\beta} \sum_m \chi_0^{dd}(i\omega_m - i\nu_i + i\nu_f, i\omega_m | \mathbf{q}) \times \chi_0^{hh}(i\omega_m + i\nu_f, i\omega_m + i\nu'_f), \quad (15)$$

whereas the contribution of the bottom diagram to $\chi_{i,f,f,i}^{(4)}(i\nu_i, i\nu_f, i\nu'_f, i\nu'_i)$ is equal to

$$-\frac{1}{\beta} \sum_m \chi_0^{hh}(i\omega_m + i\nu_i - i\nu_f, i\omega_m) \times \chi_0^{dd}(i\omega_m - i\nu_f, i\omega_m - i\nu'_f | 0). \quad (16)$$

Here, we have introduced the bare charge susceptibilities

$$\chi_0^{dd}(i\omega_m + i\nu, i\omega_m | \mathbf{q}) = -\frac{1}{N} \sum_{\mathbf{k}} G_d(\mathbf{k} + \mathbf{q}, i\omega_m + i\nu) \times G_d(\mathbf{k}, i\omega_m), \quad (17)$$

$$\chi_0^{hh}(i\omega_m^h + i\nu, i\omega_m^h) = -G_h(i\omega_m^h + i\nu)G_h(i\omega_m^h), \quad (18)$$

and $i\omega_m^h \equiv i\omega_m - E_h$. Since the core-hole propagator is local, the bottom diagram in Fig. 3 does not depend on the photon wave vector and hence can only contribute to momentum-independent background effects as evident in Eq. (16). The first diagram does depend on the transferred momentum $\mathbf{q} = \mathbf{k}_i - \mathbf{k}_f$. Since in the present study, we are interested in the energy and wave-vector dependence of the RIXS response,

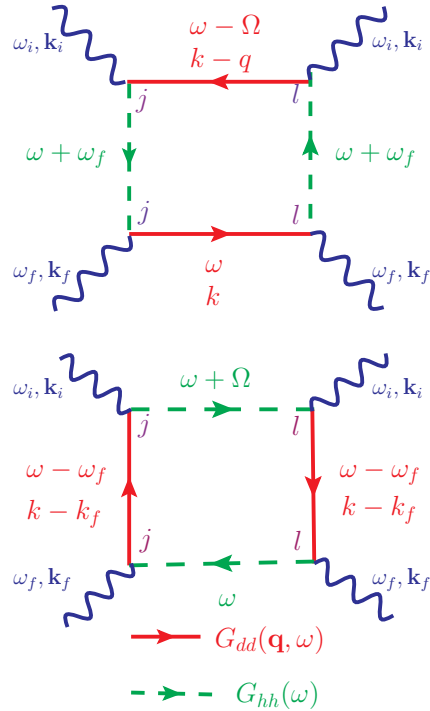


FIG. 3. (Color online) Bare loop contribution to the four-particle correlation function corresponding to the direct RIXS process. The bottom diagram gives a momentum-independent contribution (see text) to the RIXS process and hence will be neglected in this calculation.

we neglect all such momentum-independent contributions. The technical reason behind neglecting these terms is that the momentum independent contributions are the local ones and hence they include all types of many body scattering processes. Hence they can only be derived from the solution of the single-impurity problem for the four-particle correlation function $\chi^{(4)}$ (which involves multiparticle vertices and many more complications) and at this moment we do not have well developed approach for this even in the simplified Falicov-Kimball model.

Analytic continuation to real frequencies of the bare diagram in Fig. 3(a) gives the following contribution to the RIXS cross section:

$$-\frac{1}{2\pi^2} \int_{-\infty}^{+\infty} d\omega [f(\omega) - f(\omega + \Omega)] \chi_0^{hh}(\omega^- + \omega_i, \omega^+ + \omega_i) \times \text{Re} [\chi_0^{dd}(\omega^-, \omega^- + \Omega|\mathbf{q}) - \chi_0^{dd}(\omega^+, \omega^- + \Omega|\mathbf{q})], \quad (19)$$

where $f(\omega) = 1/[\exp(\beta\omega) + 1]$ is the Fermi function and

$$\chi_0^{hh}(\omega^- + \omega_i, \omega^+ + \omega_i) = -|G_h(\omega^+ + \omega_i^h)|^2. \quad (20)$$

Here, $\omega_{i,f}^h = \omega_{i,f} - E_h$ is the incident and scattered photon energy measured with respect to the core-hole energy, E_h .

Next, we introduce the renormalization of the bare charge susceptibilities through inclusion of charge vertices. In the simplest case, this can be done by inserting the two-particle charge vertex either in between the two d -hole propagators (dd channel) or between the two core-hole propagators (hh channel). Physically speaking, the incident x-ray photon creates a core-hole- d -electron pair. The excited d -electron

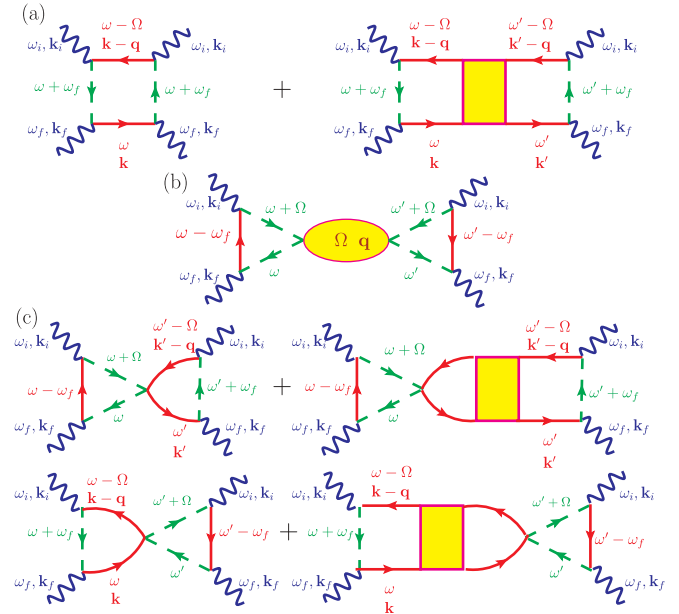


FIG. 4. (Color online) Diagrams for the renormalized four-particle correlation function $\chi^{(4)}$. Panel (a) total direct resonant scattering, (b) full exchange resonant scattering, and (c) partial exchange resonant scattering. Explicit E_h dependence of the core-hole propagator is not shown.

undergoes various inelastic scattering processes with other charge excitations in the correlated d band as well as with the electron-hole pairs created due to the presence of the core-hole potential. As a result the total scattering amplitude contains contributions from both *direct* and *indirect* scattering processes.^{1,32} The total scattering cross section, as shown in Eq. (3), is the square of the total scattering amplitude and contains four contributions. The corresponding contributions to the four-particle correlation function $\chi^{(4)}$ are represented by different rows in Fig. 4. The first row [see Fig. 4(a)] corresponds to the pure direct Coulomb processes which do not involve core-hole-band-electron scattering. The second row [see Fig. 4(b)] corresponds to full exchange scattering processes and involves dynamical screening of the core-hole potential. The last two rows [see Fig. 4(c)] describe mixed scattering arising due to the quantum mechanical interference of the direct and indirect scattering processes, which we call partial exchange.

In real experiments, the RIXS processes^{31,32} can happen either through a *direct* process, as in the case of the $L_{2,3}$ -edge $2p \rightarrow 3d$ RIXS in which the core electron is excited to an unoccupied state of the correlated valence band (d band) or through an *indirect* process, as in the case of K -edge $1s \rightarrow 4p$ RIXS in which the excited core-electron goes into an uncorrelated $4p$ band several electron volts above the Fermi level. In the present case, the excited core-electron goes to the correlated d band and the dipole selective transition $2p \rightarrow 3d$ or $3p \rightarrow 4d$ is consistent with the involvement of a $2p$ or $3p$ core hole and hence our study is related to the direct RIXS processes like L -edge or M -edge RIXS.

The sum of the two diagrams in Fig. 4(a) corresponds to the replacement in Eq. (19) of the bare charge susceptibility $\chi_0^{dd}(i\omega_m + i\nu, i\omega_m|\mathbf{q})$ by the fully renormalized charge

susceptibility $\chi^{dd}(i\omega_m + iv, i\omega_m | \mathbf{q})$, which in the case of the Falicov-Kimball model is given by

$$[\chi^{dd}(i\omega_m + iv, i\omega_m | \mathbf{q})]^{-1} = [\chi_0^{dd}(i\omega_m + iv, i\omega_m | \mathbf{q})]^{-1} + \Gamma(i\omega_m + iv, i\omega_m), \quad (21)$$

where the irreducible charge vertex⁴⁷⁻⁴⁹ is

$$\Gamma(i\omega_m + iv, i\omega_m) = \frac{1}{T} \frac{\Sigma(i\omega_m) - \Sigma(i\omega_m + iv)}{G(i\omega_m) - G(i\omega_m + iv)}. \quad (22)$$

The sum of the two diagrams in Fig. 4(a) corresponds to the *direct scattering* contribution to the RIXS process and is given by

$$-\frac{1}{2\pi^2} \int_{-\infty}^{+\infty} d\omega [f(\omega) - f(\omega + \Omega)] |G_h(\omega^+ + \omega_i^h)|^2 \times \text{Re} [\chi^{dd}(\omega^-, \omega^- + \Omega | \mathbf{q}) - \chi^{dd}(\omega^+, \omega^- + \Omega | \mathbf{q})]. \quad (23)$$

The contribution of the diagram in Fig. 4(b), which we label as the *full exchange scattering* process to the four-particle correlation function, $\chi_{i,f,f,i}^{(4)}(iv_i, iv_f, iv'_f, iv'_i)$, on the imaginary axis is given by

$$Q_d^2 \Lambda(iv_i, iv_f, iv_i - iv_f) \Lambda(iv'_i, iv'_f, iv_i - iv_f) \times \chi^{dd}(iv_i - iv_f, \mathbf{q}). \quad (24)$$

In this equation,

$$\begin{aligned} \chi^{dd}(iv, \mathbf{q}) &= \frac{1}{\beta} \sum_m \chi^{dd}(i\omega_m + iv, i\omega_m | \mathbf{q}) \\ &= \frac{i}{2\pi} \int_{-\infty}^{+\infty} d\omega [\chi^{dd}(\omega^+, \omega + iv | \mathbf{q}) \\ &\quad - \chi^{dd}(\omega^-, \omega + iv | \mathbf{q}) + \chi^{dd}(\omega - iv, \omega^+ | \mathbf{q}) \\ &\quad - \chi^{dd}(\omega - iv, \omega^- | \mathbf{q})] f(\omega) \end{aligned} \quad (25)$$

is the dynamical charge susceptibility and Λ satisfies

$$\begin{aligned} \Lambda(iv_i, iv_f, iv_i - iv_f) &= -\frac{1}{\beta} \sum_m G_h(i\omega_m + iv_i - E_h) \\ &\quad \times G_d(i\omega_m) G_h(i\omega_m + iv_f - E_h). \end{aligned} \quad (26)$$

It is important to mention that in the derivation of the full exchange scattering process contribution to RIXS in Eq. (24), we have approximated the core-hole-*d*-hole charge vertex by the core-hole-*d*-hole interaction Q_d under the Hartree-Fock approximation, which is exact to leading order. After analytic continuation to real frequencies, the corresponding contribution to the RIXS cross section is equal to

$$\begin{aligned} \frac{Q_d^2}{\pi} \text{Im} [\Lambda(\omega_i + i\delta, \omega_f + i\delta, \Omega + i\delta) \\ \times \Lambda(\omega_i - i\delta, \omega_f - i\delta, \Omega + i\delta) \chi^{dd}(\Omega + i\delta, \mathbf{q})], \end{aligned} \quad (27)$$

where $\Lambda(\omega_i \pm i\delta, \omega_f \pm i\delta, \Omega + i\delta)$ is given by

$$\begin{aligned} \frac{1}{\pi} \int_{-\infty}^{+\infty} d\omega f(\omega) [G_h(\omega^\pm + \omega_i^h) G_h(\omega^\pm + \omega_f^h) \text{Im} G_d(\omega^+) \\ + G_d(\omega^\mp - \omega_i) G_h(\omega^\mp - \Omega - E_h) \text{Im} G_h(\omega^+ - E_h) \\ + G_d(\omega^\mp - \omega_f) G_h(\omega^\pm + \Omega - E_h) \text{Im} G_h(\omega^+ - E_h)]. \end{aligned} \quad (28)$$

For large core-hole energy, E_h , we need to keep only the first term that has a small difference of energies $\mu + \omega_{i,f} - E_h$ and can safely neglect the other two terms containing large differences in energies ($\mu - E_h$ and $\mu + \Omega - E_h$, respectively). We then obtain the contribution from the full exchange processes as

$$\frac{Q_d^2}{\pi} |\bar{\Lambda}(\omega_i + i\delta, \omega_f + i\delta)|^2 \text{Im} \chi^{dd}(\Omega + i\delta | \mathbf{q}), \quad (29)$$

where

$$\begin{aligned} \bar{\Lambda}(\omega_i + i\delta, \omega_f + i\delta) &= \frac{1}{\pi} \int_{-\infty}^{+\infty} d\omega f(\omega) G_h(\omega^+ + \omega_i^h) \\ &\quad \times G_h(\omega^+ + \omega_f^h) \text{Im} G_d(\omega^+), \end{aligned} \quad (30)$$

$$\begin{aligned} \text{Im} \chi^{dd}(\Omega + i\delta, \mathbf{q}) &= \frac{1}{2\pi} \int_{-\infty}^{+\infty} d\omega [f(\omega) - f(\omega + \Omega)] \\ &\quad \times \text{Re} [\chi^{dd}(\omega^-, \omega^- + \Omega | \mathbf{q}) \\ &\quad - \chi^{dd}(\omega^+, \omega^- + \Omega | \mathbf{q})]. \end{aligned} \quad (31)$$

Apart from the *direct* and *full exchange* resonant scattering processes, we also have processes, termed as the *partial exchange* processes, as shown in Fig. 4(c). The sum of their contributions to the four-particle correlation function, $\chi_{i,f,f,i}^{(4)}(iv_i, iv_f, iv'_f, iv'_i)$, on the imaginary axis is equal to

$$\begin{aligned} -Q_d \frac{1}{\beta} \sum_m \chi^{dd}(i\omega_m, i\omega_m + iv_i - iv_f | \mathbf{q}) \\ \times [G_h(i\omega_m + iv'_i - E_h) \Lambda(iv_i, iv_f, iv_i - iv_f) \\ + G_h(i\omega_m + iv_i - E_h) \Lambda(iv'_i, iv'_f, iv'_i - iv'_f)]. \end{aligned} \quad (32)$$

After analytic continuation to real frequencies, we obtain the following partial exchange contribution to the RIXS response:

$$\begin{aligned} -\frac{Q_d}{\pi^2} \text{Re} \left\{ \bar{\Lambda}(\omega_i + i\delta, \omega_f + i\delta) \int_{-\infty}^{+\infty} d\omega [f(\omega) - f(\omega + \Omega)] \right. \\ \times G_h(\omega^- + \omega_i - E_h) \text{Re} [\chi^{dd}(\omega^-, \omega^- + \Omega | \mathbf{q}) \\ \left. - \chi^{dd}(\omega^+, \omega^- + \Omega | \mathbf{q}) \right\}. \end{aligned} \quad (33)$$

It is interesting to mention that for the *L*-edge RIXS process, which we consider in the present study, pure direct resonant scattering processes are overwhelmingly dominant over the resonant exchange (both full and partial) processes. Besides the diagrams considered above, we could also have considered other contributions to the charge vertex between the two core-hole propagators which produce diagrams like the parquet diagram in Fig. 5. From a simple power counting argument, we can show that the contribution of such diagrams goes at least as an inverse power of the dimension of the lattice, d . So, in the limit of $d \rightarrow \infty$, they all have vanishing contributions except in the case when they are all local (and we neglect all such momentum-independent contributions).

The nonresonant part of the RIXS response is found to be related to the density-density correlation function. To be precise, the nonresonant part is proportional to the dynamical structure factor,⁵⁰ $S(\mathbf{q}, \Omega)$, which is given by

$$S(\mathbf{q}, \Omega) = -\frac{1}{\pi} [1 + n_B(\Omega, T)] \text{Im} \chi^{dd}(\Omega + i\delta | \mathbf{q}), \quad (34)$$

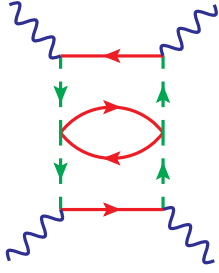


FIG. 5. (Color online) Parquet diagrams with vanishing contribution to the RIXS response in the limit of infinite dimension.

where $n_B(\omega, T) = 1/[\exp(\beta\omega) - 1]$ is the Bose distribution function and $\chi^{dd}(\Omega + i\delta|\mathbf{q})$ is the dynamic charge susceptibility⁴⁸ [see Eq. (31)] of the system.

IV. RIXS RESPONSE FOR THE HALF-FILLED MOTT INSULATOR

As has been already stated, the Falicov-Kimball model at half-filling ($\langle n_d \rangle = \langle n_f \rangle = 0.5$, $\mu = U/2$, and $E_f = 0$) on a hypercubic lattice shows a Mott insulating ground state for $U > U_c = \sqrt{2}$. We choose $U = 2.0$, $Q_d = Q_f = 2.5$, and $T = 0.1$ in units of effective hopping amplitude t^* and from here onwards we choose $t^* = 1$. This choice of U gives a small “gap” ($\Delta_{\text{gap}} \simeq 0.25$ in units of t^*) Mott insulator. Note that for the $d \rightarrow \infty$ hypercubic lattice DOS there is no true gap as there is an exponentially small DOS inside the gap.

In Fig. 6, we show the spectral function for the itinerant species, $A_d(\omega)$, as well as for the core-hole, $A_h(\omega - E_h)$. $A_d(\omega)$ clearly shows a gap (Mott gap) at the Fermi level ($\omega = 0$) while $A_h(\omega - E_h)$ also shows a gap at some other frequency (at $\omega = E_h - 1.2$ in this example) and the origin of this gap is related to the same strong correlation effects that gives rise to the Mott gap in the itinerant species spectral function. Surprisingly, the gap structure is quite different for the core hole, which is arising due to the asymmetry in the

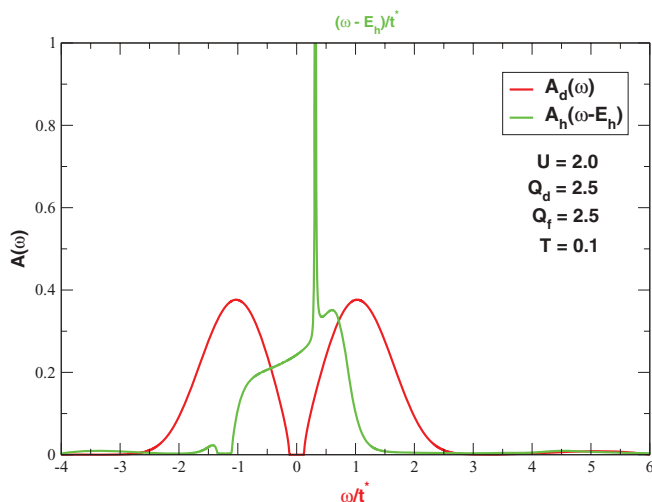


FIG. 6. (Color online) Spectral function for the d hole, $A_d(\omega)$, and the core hole, $A_h(\omega - E_h)$. For $A_h(\omega - E_h)$, the frequency is measured with respect to the core-hole energy, E_h , as shown in the top horizontal axis.

Green’s function for large E_h . $A_h(\omega - E_h)$ is dominated by a broad feature, arising from the projection of $G^>(t)$ onto the $n_h = 0, n_f = 0$ configuration, along with a very sharp peak arising from the projection onto the $n_h = 0, n_f = 1$ configuration in the final state.⁴²

From the knowledge of the itinerant electron propagator, $G_d(\mathbf{q}, \omega)$, core-hole propagator, $G_h(\omega - E_h)$, and the fully renormalized two-particle charge susceptibility, $\chi^{dd}(i\omega_m, i\omega_m + i\nu|\mathbf{q})$, we can calculate the RIXS response either as a function of transferred energy (Ω) for a given fixed incident photon energy, ω_i (measured with respect to the core-hole energy E_h), or as a function of ω_i for a given fixed transferred energy, Ω , for various transferred momenta \mathbf{q} of the photon. It is interesting to mention that in the limit $d \rightarrow \infty$ the momentum on the hypercubic lattice only enters through the dimensionless parameter,⁵¹

$$X(\mathbf{q}) = \lim_{d \rightarrow \infty} \frac{1}{d} \sum_{i=1}^d \cos(q_i). \quad (35)$$

So, $-1 \leq X \leq 1$ and $X = 1$ and $X = -1$ corresponds to the center, $(0, \dots, 0)$ (Γ point), and the corner, (π, \dots, π) (M point), of the Brillouin zone of a d -dimensional hypercubic lattice, respectively. It is convenient to think of this parametrization as corresponding to RIXS scattering in the diagonal $(1 \dots 1)$ direction.

First, in Fig. 7, we plot the resonant part of the RIXS response as a function of the transferred energy, Ω , for various transferred momenta, X , for three different incident photon energies, $\omega_i = -0.5, 0.5, 1.5$. For $\omega_i = -0.5$, the core electron, excited by the incident x-ray photon, is injected into the lower Hubbard band and the inelastic relaxation processes can happen only within the lower Hubbard band that is evident in the single-peak structure in the RIXS response in Fig. 7(a). At the M point, the peak is large and well defined but as we go towards the middle of the Brillouin zone ($X = 0.0$), the peak gets broadened and the position of the peak does not disperse significantly. Finally, as we approach the zone center, the position of the peak disperses significantly and moves towards lower energy, also at the same time the peak gets more and more well defined though the integrated spectral intensity under the peak gradually diminishes and eventually goes to zero at the center of the Brillouin zone ($X = 1$). This is related to the vanishing of the uniform charge susceptibility (due to the fact that we exactly include the screening dynamics for the conduction electrons and long-wavelength charge excitations are fully screened).

As we increase the incident photon energy above the Mott gap, we start to excite the system into the upper Hubbard band and in Fig. 7(b), we show a characteristic response when the incident photon, with energy $\omega_i = 0.5$, excites a core electron into the bottom of the upper Hubbard band. Near the zone corner the response still shows a single-peak structure albeit shifted by the insulating gap, but as we go towards the zone center, the response at low energy develops a very narrow secondary peak separated from the broad main peak by the Mott gap. The low-energy peak arises due to relaxation processes within the upper Hubbard band and is nondispersive in nature, whereas the high-energy peak arises due to relaxation processes across the Mott gap into the lower

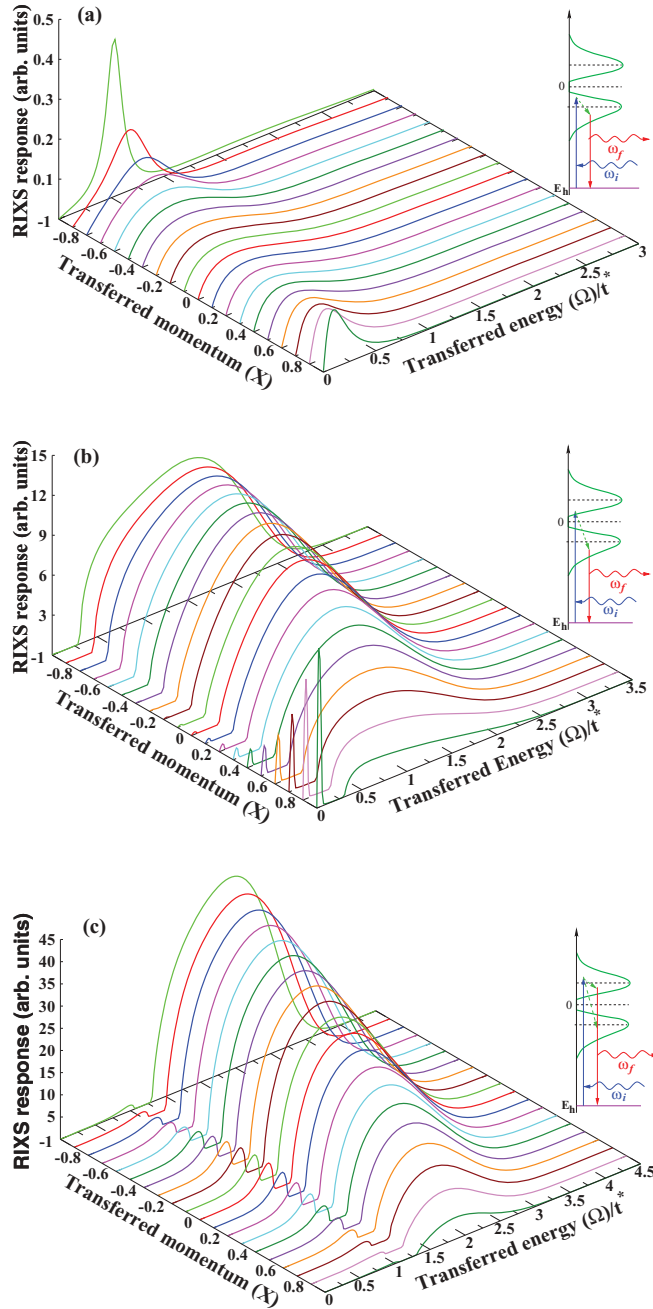


FIG. 7. (Color online) RIXS response as a function of transferred energy (Ω) for various fixed transferred momenta (X) with three different incident photon energies, ω_i . (a) The incident photon energy is at the lower Hubbard band, in (b), at the bottom of the upper Hubbard band, and in (c), it is at the middle of the upper Hubbard band. The inset of each plot schematically depicts the possible RIXS relaxation processes. The chosen parameters are $U = 2.0$, $Q_d = Q_f = 2.5$, and $T = 0.1$. Note, the signal vanishes exactly at $X = 1$ due to screening.

Hubbard band and is found to be dispersive over the Brillouin zone. With further increase in the incident photon energy to $\omega_i = 1.5$ the low-energy peak and the spectral weight under it, as shown in Fig. 7(c), grows significantly and is visible for all momenta along the $(1 \cdot \cdot \cdot 1)$ direction. However, the intensity of this low-energy peak shows nonmonotonic behavior: it

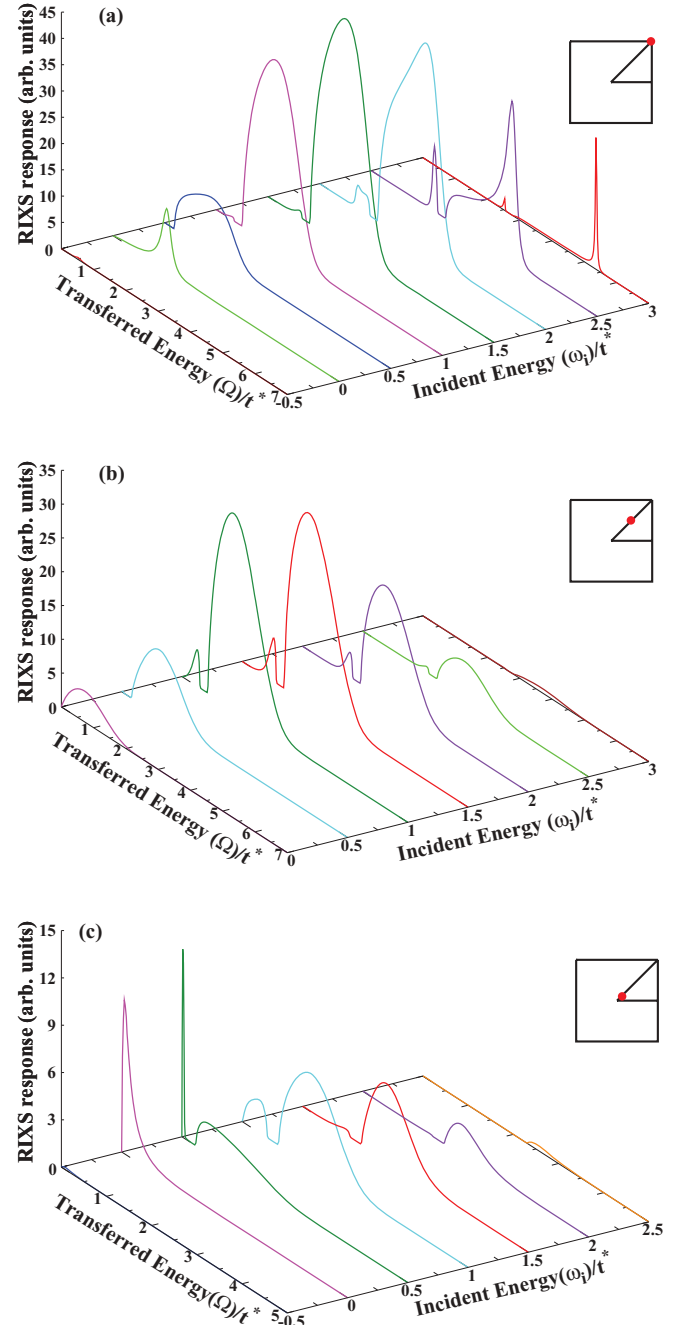


FIG. 8. (Color online) RIXS response as a function of transferred energy (Ω) for various fixed incident photon energies, ω_i , varying from the bottom of the lower Hubbard band to the top of the upper Hubbard band for three different momenta, X : (a) zone corner (M point) $X = -1$, (b) somewhere in the middle of the zone $X = 0$, and (c) near the zone center $X = 0.9$. Inset of each plot shows the position of each X inside the first Brillouin zone. All other parameters are the same as in Fig. 7.

first increases up to $X = 0$ and then starts to decrease and eventually vanishes at the zone center, $X = 1$. On the other hand, the intensity of the high-energy peak monotonically decreases as well as disperses to lower energies as we go from the zone corner towards the zone center and eventually vanishes at the center of the Brillouin zone.

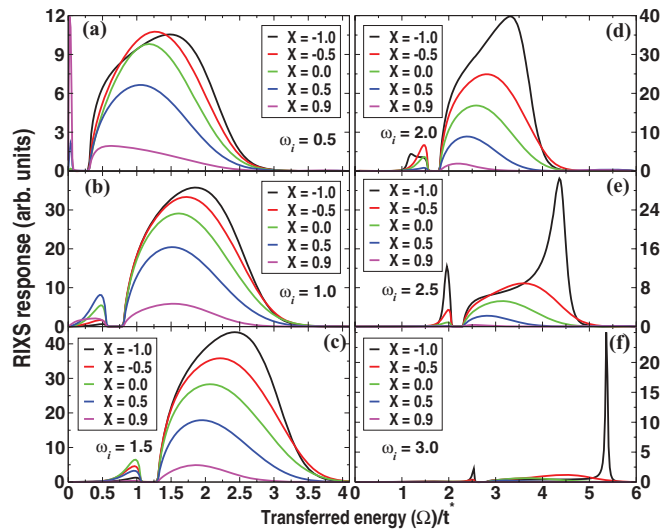


FIG. 9. (Color online) Systematic evolution of the RIXS response as a function of transferred energy (Ω) for six incident photon energies from the bottom of the upper Hubbard band: $\omega_i = 0.5$ (a) to the top of the upper Hubbard band $\omega_i = 3.0$ (f). The dispersive nature of the high-energy peak (Mott gap excitation) is noticeable. All other parameters are the same as in Fig. 7.

In Figs. 8(a)–8(c), we show the systematic evolution of the RIXS response for three transferred momenta $X = -1, 0$, and 0.9 , respectively. As we vary the incident photon energy, the energy of the excited core electron varies from the bottom of the lower Hubbard band to the top of the upper Hubbard band and the RIXS response evolves from a single-peak structure to a two-peak structure. Finally, when the excited core electron goes into states beyond the edges of the Hubbard bands the response vanishes quickly due to an exponential reduction of the density of states that in effect drastically reduces the phase space for inelastic scattering. Also, the overall response decreases as we go towards the zone center.

In Fig. 9, we show a more detailed and systematic evolution of the RIXS response with varying energy of the incident photon, which excites the core electron into the upper Hubbard band. As we can clearly see, the low-energy peak, which arises due to relaxation processes within the upper Hubbard band, does not disperse over the Brillouin zone (except its intensity varies), whereas the high-energy peak (which arises due to relaxation processes across the Mott gap) shows significant dispersion over the Brillouin zone. Similar features like the two-peak structure and the dispersive nature of the high-energy peak have been observed in the RIXS measurements on a Mott insulator $\text{Ca}_2\text{CuO}_2\text{Cl}_2$ by Hassan *et al.*⁵ and have been attributed to strong correlation effects.

It is interesting to mention that at zero temperature in the half-filled Mott-insulating ground state, the chemical potential as well as the Fermi level lies within the Mott gap, which results in a completely filled lower Hubbard band (LHB) and a completely empty upper Hubbard band (UHB). As a result, when the incident photon energy is within the LHB, the RIXS response will vanish due to the unavailability of any unoccupied state in the LHB to which the core electron can

be excited and when the incident photon energy is within the upper Hubbard band the RIXS response will have a single-peak structure arising due to charge transfer excitations across the gap. At finite temperature, some of the states near the top of the LHB get thermally excited across the gap and occupy the bottom of the UHB. So, at finite temperature, if the incident photon excites a core-electron into the unoccupied states of the LHB, the RIXS response will have a single-peak structure corresponding to relaxation processes involving LHB states. If the excited core-electron goes into the unoccupied states of the UHB then it can undergo relaxation processes either with the thermally excited UHB electrons occupying the bottom of the UHB giving rise to a low-energy nondispersive peak or through charge transfer excitations across the gap giving rise to a dispersive high-energy peak. Also, the whole structure gets shifted to higher energy with increasing incident photon energy due to the fact that with increasing incident photon energy the transferred energy must also increase in order to have resonant scattering from the thermally excited states, which predominantly occupy the bottom of the UHB and the top of the LHB. In the case of a large gap Mott insulator, as will be shown in a following section (see Sec. VI), the intraband relaxation processes from the thermally excited states are negligibly small compared to the excitations across the Mott gap.

Finally, in Figs. 10(a)–10(c), we plot the RIXS response as a function of the incident photon energy, ω_i , for various fixed transferred photon energies, Ω , for three transferred momenta $X = -1, 0$, and 0.9 , respectively. For small Ω , the RIXS response shows a two-peak structure in ω_i , which corresponds to the relaxation processes within the individual bands (upper and lower Hubbard bands). As we increase Ω an additional peak develops between the two peaks. This peak corresponds to the interband relaxation processes across the Mott gap and grows very rapidly with increasing Ω , while the other two peaks decrease in intensity until we are finally left with a lone peak. Hence, we can infer that in a Mott insulator, interband relaxation processes across the Mott gap are dominant over intraband relaxation processes. Also, as we go from the zone corner to the zone center, the intensity of the peaks decreases as in Fig. 7.

We also have calculated the dynamical structure factor, $S(\mathbf{q}, \Omega)$, which is proportional to the nonresonant part of the RIXS response.⁴⁸ In Fig. 11, we plot $S(\mathbf{q}, \Omega)$ for the small-gap insulator at $T = 0.1$. Near the zone corner, $S(\mathbf{q}, \Omega)$ has a broad charge transfer peak but as we go towards the zone center, a secondary peak develops near $\Omega = 0$ and the integrated spectral weight under the charge transfer peak decreases. Finally, exactly at the zone center ($X = 1$), the charge transfer peak completely vanishes while the peak around $\Omega = 0$ turns into a δ function, which again arises due to the vanishing of the uniform charge susceptibility at finite frequency. This behavior is quite different from the resonant response where the two-peak structure is most prominent near the zone corner and also the charge transfer peak in $S(\mathbf{q}, \Omega)$ is much smaller and much less dispersive than the high-energy peak observed in the resonant response and most importantly the position of the peak cannot be identified with any particular x-ray transition process.

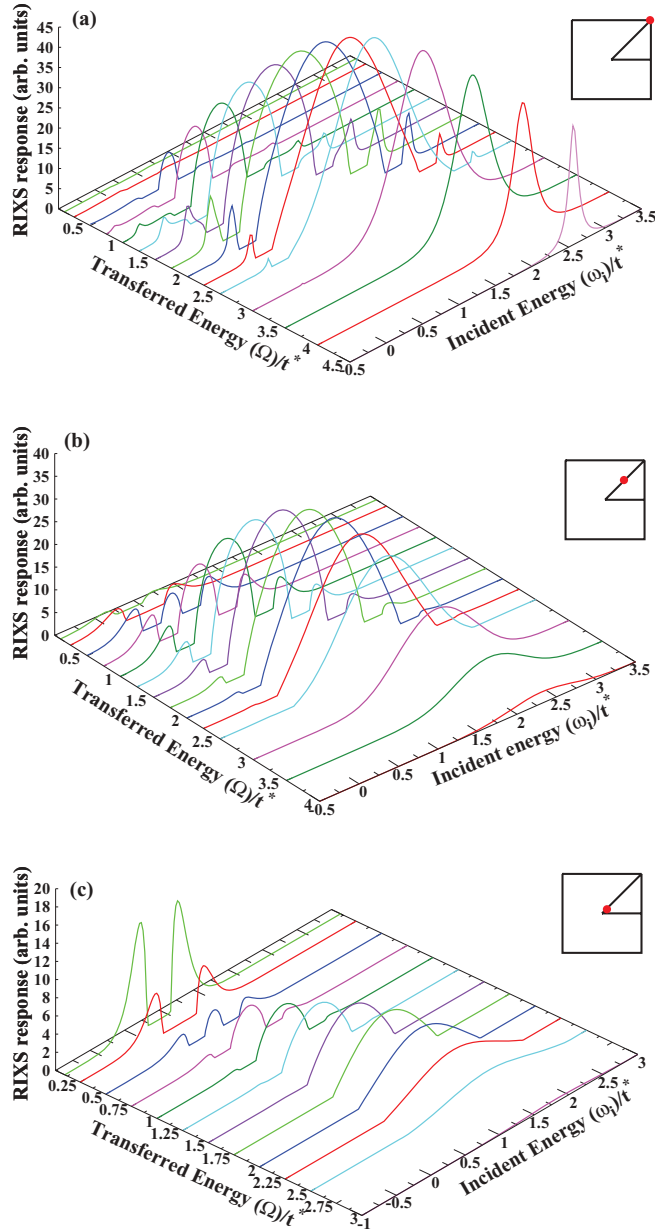


FIG. 10. (Color online) RIXS response as a function of incident energy, ω_i , for various fixed transferred energies, Ω , for three characteristic transferred momenta, X : (a) zone corner (M point) $X = -1$, (b) in the middle of the zone $X = 0$, and (c) near the zone center $X = 0.9$. The inset of each plot shows the position of each X inside the first Brillouin zone. All other parameters are the same as in Fig. 7.

V. CORE-HOLE BROADENING EFFECTS

In the preceding section, we have not included any additional core-hole lifetime broadening effects that can arise due to various nonradiative Auger and fluorescence effects and are important in the transition metal RIXS processes (we only included the intrinsic many-body effects in determining the core-hole lifetime). In our calculation, we can easily include such effects by simply making the core-hole energy E_h complex, i.e., by making the transformation $E_h \rightarrow E_h - i\Gamma$ into the *retarded* Green's function, $G_h^r(t) = \Theta(t)[G_h^>(t) - G_h^<(t)]$,

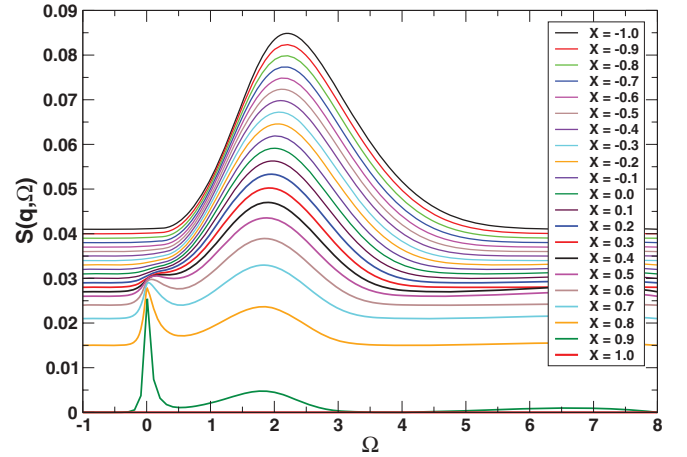


FIG. 11. (Color online) Dynamical structure factor, $S(\mathbf{q}, \Omega)$, for $U = 2.0$ and $T = 0.1$. Note, it vanishes for $X = 1$ due to screening.

and $E_h \rightarrow E_h + i\Gamma$ into the *advanced* Green's function, $G_h^a(t) = \Theta(-t)[G_h^<(t) - G_h^>(t)]$, respectively. Here, $\Gamma = \hbar/\tau$ with τ being the core-hole lifetime and for most materials, $\Gamma \sim 100\text{--}400$ meV (1–3 in units of t^*).

While this may seem like an *ad hoc* procedure, microscopic calculation of Auger lifetimes in condensed matter systems is beyond the scope of this work, and this broadening effect on the core hole spectral function is important to determine whether all of the features calculated above survive when the core hole spectral function is further broadened. Hence it is an important element in any analysis.

First, in Fig. 12, we show the systematic evolution of the core-hole spectral function, $A_h(\omega - E_h)$, with additional core-hole broadening effects parameterized by Γ . With increasing Γ , the height of the sharp peak in $A_h(\omega - E_h)$ reduces, while its width significantly broadens but the asymmetrical nature of the structure is largely retained. Also, the Mott gap in the $\Gamma = 0.0$ case (near $\omega - E_h \sim -1.0$) is replaced by a dip in the spectral function and the tail of $A_h(\omega - E_h)$ increases with increasing Γ .

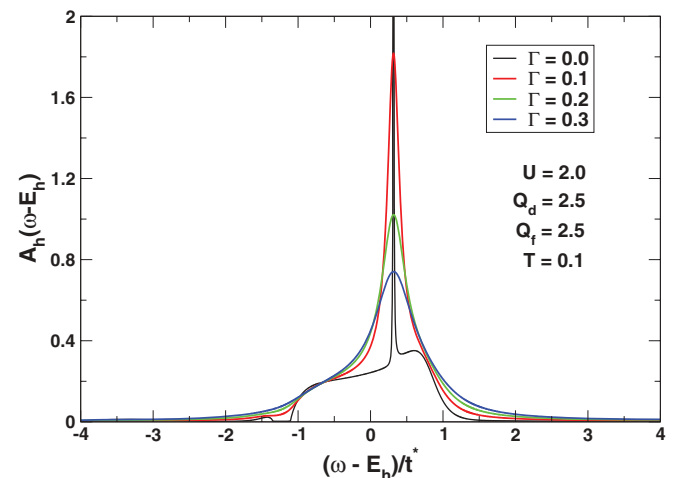


FIG. 12. (Color online) Core-hole spectral function, $A_h(\omega - E_h)$, evolution with core-hole broadening parameter, Γ . All other parameters are same as in Fig. 7.

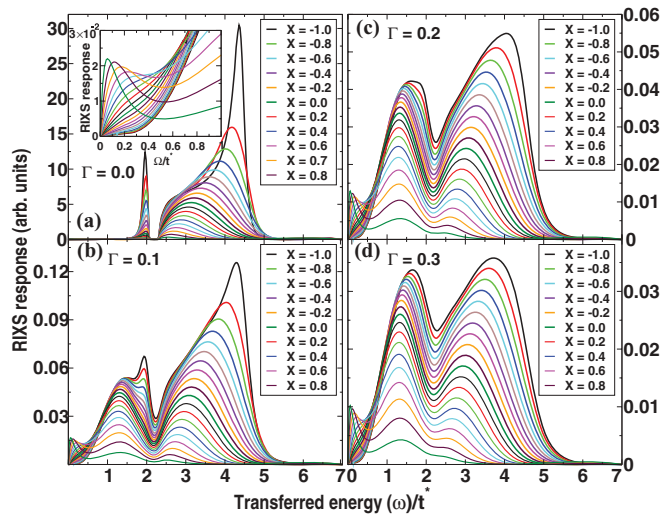


FIG. 13. (Color online) Evolution of the RIXS response as a function of the transferred energy, Ω , and various fixed transferred momenta, X , for incident photon energy $\omega_i = 2.5$ with various core-hole lifetime broadening parameters, Γ . (a) Response for $\Gamma = 0$ and the inset of panel (a) shows the quasielastic peak in the blown up far-infrared region. (b)–(d) Responses for broadening parameters much smaller ($\Gamma = 0.1$), comparable ($\Gamma = 0.2$), and larger ($\Gamma = 0.3$) than the Mott insulating gap $\Delta_{\text{gap}} \sim 0.25$. All other parameters are the same as in Fig. 7. For all the four sets, calculations have been performed from $X = -1.0$ (top most curve) to $X = 0.9$ (bottom most curve) with a step size of 0.1 for the momentum variable X .

In Figs. 13(a)–13(d), we show a detailed evolution of the RIXS response with various broadening parameters, Γ (measured in units of t^*). We choose four characteristic parameters $\Gamma = 0.0, 0.1, 0.2$, and 0.3 corresponding to no broadening, much smaller, comparable, and larger broadening compared to the intrinsic Mott-insulating gap in the system, respectively. All other parameters chosen are the same as in the previous case. In Fig. 13(a), we plot the RIXS response without any additional core-hole broadening effect and the response shows a clear two-peak structure with the peaks well separated by the Mott gap. The low-energy peak is nondispersive but the high-energy peak is highly dispersive in momenta and also changes its shape significantly as we go from the zone corner to the zone center. Also, interestingly, close to the zone center a quasielastic peak develops in the far-infrared region. The intensity as well as sharpness of this peak increases as we go towards the zone center.

From the detailed analysis of the weights of the different scattering processes presented in Fig. 4 for the total RIXS response, we find that the main two-peak structure and its rather strong momentum dependence originates from the direct scattering processes described by Eq. (24) [see Fig. 4(a)]. Contribution from the full exchange (indirect) processes in Eq. (29) [see Fig. 4(b)] is much smaller and are mainly responsible for the quasielastic peak, which corresponds to the dynamical structure factor, $S(\mathbf{q}, \Omega)$ [see Fig. 11].

The presence of additional core-hole lifetime broadening effects strongly suppresses the direct contribution. We no longer see a clear gap structure in Figs. 13(b)–13(d) but the two-peak structure is still clearly evident for all momenta. Also

the high-energy peak still remains dispersive throughout the Brillouin zone, while the low-energy peak is more or less nondispersive in nature as in the case with no additional core-hole broadening. The height of the quasielastic peak close to the zone center slightly decreases with increasing Γ , which is related to the weak dependence of the $\bar{\Lambda}$ prefactor in Eq. (29) on Γ , while its width and dispersive features remains similar to the $\Gamma = 0.0$ case. However, in a real experiment, finite resolution and the resolution broadened tail of the huge elastic peak will mask such quasielastic features which will then not be observable. So, the presence of additional core-hole broadening effects can significantly modify the overall response, but the most important qualitative features, like the two-peak structure and the dispersive features of these peaks remain similar.

VI. RESPONSE AWAY FROM HALF-FILLING

Finally, we consider a Mott insulator at arbitrary filling to examine the breaking of particle-hole symmetry in the RIXS response. We choose $U = 4.0$, $Q_d = Q_f = 5.0$, $\langle n_f \rangle = 0.25$, $\langle n_d \rangle = 0.75$, and $T = 0.1$. This choice of parameters gives a large-gap Mott insulator ($\Delta_{\text{gap}} \sim 1.8$ in units of t^*). In Fig. 14(a), we show the d -hole spectral function, $A_d(\omega)$, as well as the core-hole spectral function, $A_h(\omega - E_h)$, with ($\Gamma = 1.0$) and without ($\Gamma = 0.0$) core-hole broadening effects. $A_d(\omega)$ is dominated by two asymmetrical peaks separated by a large gap at the Fermi level. $A_h(\omega - E_h)$ [without any additional core-hole broadening effect ($\Gamma = 0.0$)] shows two very closely spaced sharp peaks on top of a broad feature but with the inclusion of large core-hole broadening ($\Gamma = 1.0$), the whole structure gets drastically modified and $A_h(\omega - E_h)$ resembles a broad nearly symmetrical single peak.

In Fig. 14(b), we show the RIXS response as a function of the transferred energy, Ω , for various fixed transferred momenta, X , for $\Gamma = 0.0$. The response in this case is overwhelmingly dominated by a huge peak arising due to relaxation processes across the Mott gap into the LHB, while the intraband (within the UHB) relaxation processes as shown in the inset of Fig. 14(b) are much weaker than the interband processes. As already has been mentioned in Sec. IV, in a large-gap Mott insulator, the density of thermally excited states, which occupy the bottom of the UHB, is extremely small and hence cannot provide any significant relaxation to the core electrons excited to the UHB. The high-energy peak, just as in the case of particle-hole symmetric half-filled case, shows significant dispersion with transferred momentum—the peak disperses outwards in energy as we go from the zone center towards the zone corner. Finally, we study the RIXS response in the presence of finite core-hole broadening. In Fig. 14(c), we show results for a typical broadening (of the order of the Mott gap) $\Gamma = 1.0$. The first noticeable feature is the reemergence of the *two-peak* structure. This is mainly due to a huge suppression of the sharp resonating peak in $A_h(\omega - E_h)$, as can be observed in Fig. 14(a), which in effect drastically reduces the resonant response across the Mott gap by six orders of magnitude. The high-energy peak still shows significant dispersion across the entire Brillouin zone and

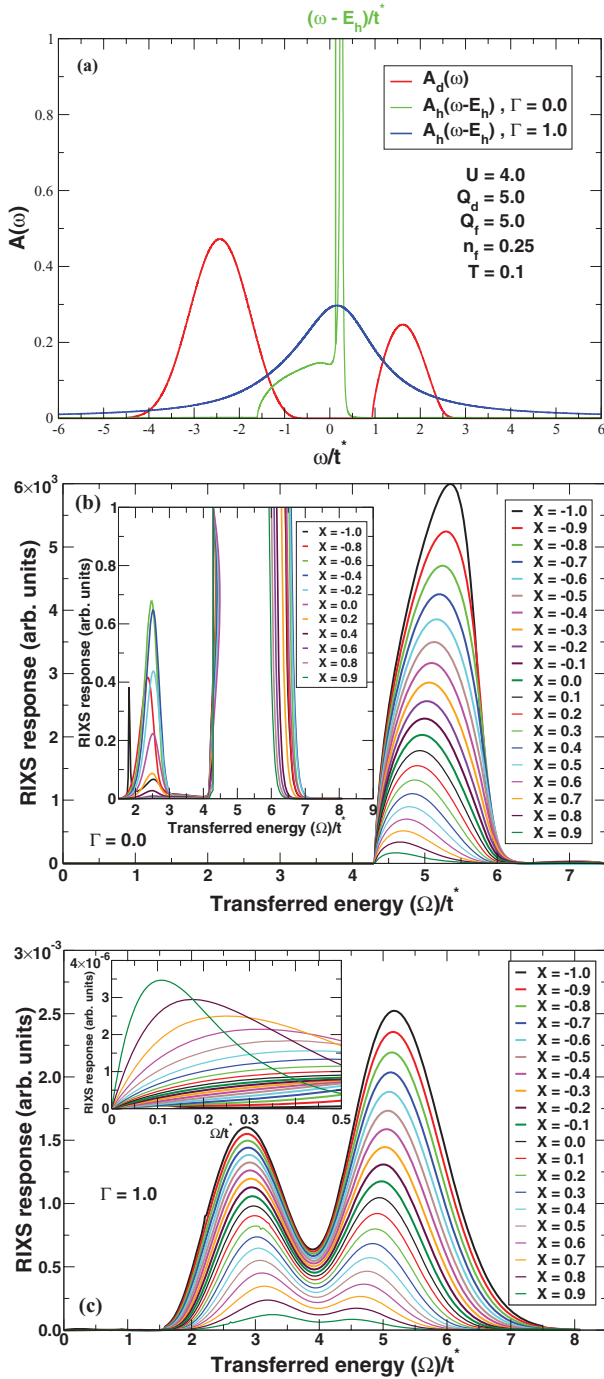


FIG. 14. (Color online) (a) d -hole spectral function, $A_d(\omega)$, as well as the core-hole spectral function, $A_h(\omega - E_h)$, with ($\Gamma = 1.0$, blue line) and without ($\Gamma = 0.0$, green line) core-hole broadening effects in a particle-hole asymmetric large gap Mott insulator. For the core-hole spectral function, energy is measured with respect to the core-hole energy, E_h , i.e., $\omega \rightarrow \omega - E_h$. (b) and (c) RIXS response as a function of the transferred energy, Ω , for various fixed transferred momenta, X , without [$\Gamma = 0.0$ (b)] and with [$\Gamma = 1.0$ (c)] core-hole broadening effects for incident photon energy (measured with respect to E_h) $\omega_i = 3.5$. Magnified response in the inset of panel (b) clearly shows a *two-peak* structure and the inset of panel (c) shows the quasielastic peak in the blown up far-infrared region. The parameters used for this plot are $U = 4.0$, $Q_d = Q_f = 5.0$, $T = 0.1$, and $n_f = 0.25$, $n_d = 0.75$.

the low-energy peak also shows dispersive features. Also, as shown in the inset of Fig. 14(c), a very weak quasielastic peak similar to the half-filled case emerges due to the full exchange (indirect) processes.

VII. CONCLUSIONS

In conclusion, we have studied the RIXS response in a Mott insulator which is modeled by the Falicov-Kimball model. We have considered both the particle-hole symmetric half-filled case as well as the general particle-hole asymmetric case. We find that when the incident photon energy is lying within the upper Hubbard band, the resonant response shows a two-peak structure arising from the intraband (low-energy peak) and interband (high-energy peak) relaxation processes (as expected since the gap is larger but the temperature is the same as before). The high-energy peak is found to be much larger and sometimes overwhelmingly larger (away from half-filling case) than the low-energy peak and shows dispersive features throughout the entire Brillouin zone, while the low-energy peak remains more or less nondispersive. Such distinctive features have already been observed in a large class of transition metal K -edge RIXS responses in a wide class of oxide materials and have been attributed to the nonlocal nature of the Mott gap excitations.

We also have considered moderately large core-hole broadening effects (due to finite Auger lifetime of the core hole) on the RIXS response and we see that despite significant change in the RIXS response many interesting qualitative features like the two-peak structure and the dispersive nature of the high-energy peak remains more or less intact. The quasielastic feature near the zone center, which originates from the pure full exchange (indirect) processes, becomes comparable to the other two peaks. However, this peak will be completely masked by the resolution limited tail of the elastic peak (and cannot be observed in any current experiments). For the half-filled case, we also have calculated the dynamical structure factor, $S(\mathbf{q}, \Omega)$, which is proportional to the nonresonant part of the response. $S(\mathbf{q}, \Omega)$ is either dominated by a very weakly dispersive charge transfer peak when the transferred photon momentum, X , is near the zone corner or by a narrow peak around $\Omega = 0$, which corresponds to the quasielastic peak in RIXS from the full exchange (indirect) processes, when the momentum is close to the zone center. Exactly at the zone center $S(\mathbf{q}, \Omega)$ vanishes for finite frequencies, while the narrow peak becomes a delta function peak. We believe, features like the two-peak structure and the dispersive natures of the charge transfer peak are generic features of the RIXS response in a Mott insulator and similar features are expected to be observed in calculations based on the more realistic Hubbard model.

ACKNOWLEDGMENTS

This work was supported by the US Department of Energy under grant No. DE-FG02-08ER46542 for the work at Georgetown and grants Nos. DE-FG02-08ER46540 and DE-SC0007091 for the collaboration. We would like to thank Tom Devereaux and Brian Moritz for many useful discussions and a critical reading of this manuscript. We would also like to thank M. A. van Veenendaal, A. Bansil,

R. Markiewicz, J. Moreno, Z. Hussain, J. Rehr, and A. Sorini for useful discussions. J.K.F. also acknowledges support from the McDevitt bequest at Georgetown. All the

Feynman diagrams in this paper were drawn by using open source software program JAXODRAW and the original reference has been duly cited in Ref. 52.

-
- ¹L. J. P. Ament, M. van Veenendaal, T. P. Devereaux, J. P. Hill, and J. van den Brink, *Rev. Mod. Phys.* **83**, 705 (2011).
- ²J. P. Hill, C.-C. Kao, W. A. L. Caliebe, M. Matsubara, A. Kotani, J. L. Peng, and R. L. Greene, *Phys. Rev. Lett.* **80**, 4967 (1998).
- ³P. Abbamonte, C. A. Burns, E. D. Isaacs, P. M. Platzman, L. L. Miller, S. W. Cheong, and M. V. Klein, *Phys. Rev. Lett.* **83**, 860 (1999).
- ⁴K. Hämäläinen, J. P. Hill, S. Huotari, C.-C. Kao, L. E. Berman, A. Kotani, T. Idé, J. L. Peng, and R. L. Greene, *Phys. Rev. B* **61**, 1836 (2000).
- ⁵M. Z. Hasan, E. D. Isaacs, Z.-X. Shen, L. L. Miller, K. Tsutsui, T. Tohyama, and S. Maekawa, *Science* **288**, 1811 (2000).
- ⁶M. Z. Hasan, P. A. Montano, E. D. Isaacs, Z.-X. Shen, H. Eisaki, S. K. Sinha, Z. Islam, N. Motoyama, and S. Uchida, *Phys. Rev. Lett.* **88**, 177403 (2002).
- ⁷Y. J. Kim, J. P. Hill, C. A. Burns, S. Wakimoto, R. J. Birgeneau, D. Casa, T. Gog, and C. T. Venkatraman, *Phys. Rev. Lett.* **89**, 177003 (2002).
- ⁸Y. J. Kim, J. P. Hill, H. Benthien, F. H. L. Essler, E. Jeckelmann, H. S. Choi, T. W. Noh, N. Motoyama, K. M. Kojima, S. Uchida, D. Casa, and T. Gog, *Phys. Rev. Lett.* **92**, 137402 (2004).
- ⁹K. Ishii, K. Tsutsui, Y. Endoh, T. Tohyama, K. Kuzushita, T. Inami, K. Ohwada, S. Maekawa, T. Masui, S. Tajima, Y. Murakami, and J. Mizuki, *Phys. Rev. Lett.* **94**, 187002 (2005).
- ¹⁰K. Ishii, K. Tsutsui, Y. Endoh, T. Tohyama, S. Maekawa, M. Hoesch, K. Kuzushita, M. Tsubota, T. Inami, J. Mizuki, Y. Murakami, and K. Yamada, *Phys. Rev. Lett.* **94**, 207003 (2005).
- ¹¹J. P. Hill, G. Blumberg, Y. J. Kim, D. S. Ellis, S. Wakimoto, R. J. Birgeneau, S. Komiya, Y. Ando, B. Liang, R. L. Greene, D. Casa, and T. Gog, *Phys. Rev. Lett.* **100**, 097001 (2008).
- ¹²G. Ghiringhelli, N. B. Brookes, E. Annese, H. Berger, C. Dallera, M. Grioni, L. Perfetti, A. Tagliaferri, and L. Braicovich, *Phys. Rev. Lett.* **92**, 117406 (2004).
- ¹³G. Ghiringhelli, N. B. Brookes, C. Dallera, A. Tagliaferri, and L. Braicovich, *Phys. Rev. B* **76**, 085116 (2007).
- ¹⁴L. Braicovich, J. van den Brink, V. Bisogni, M. Moretti Sala, L. J. P. Ament, N. B. Brookes, G. M. De Luca, M. Salluzzo, T. Schmitt, V. N. Strocov, and G. Ghiringhelli, *Phys. Rev. Lett.* **104**, 077002 (2010).
- ¹⁵T. Inami, T. Fukuda, J. Mizuki, S. Ishihara, H. Kondo, H. Nakao, T. Matsumura, K. Hirota, Y. Murakami, S. Maekawa, and T. Endoh, *Phys. Rev. B* **67**, 045108 (2003).
- ¹⁶G. Ghiringhelli, M. Matsubara, C. Dallera, F. Fracassi, A. Tagliaferri, N. B. Brookes, A. Kotani, and L. Braicovich, *Phys. Rev. B* **73**, 035111 (2006).
- ¹⁷G. Ghiringhelli, A. Piazzalunga, C. Dallera, T. Schmitt, V. N. Strocov, J. Schlappa, L. Patthey, X. Wang, H. Berger, and M. Grioni, *Phys. Rev. Lett.* **102**, 027401 (2009).
- ¹⁸B. J. Kim, H. Ohsumi, T. Komesu, S. Sakai, T. Morita, H. Takagi, and T. Arima, *Science*, **323**, 1329 (2009).
- ¹⁹K. Ishii, I. Jarrige, M. Yoshida, K. Ikeuchi, J. Mizuki, K. Ohashi, T. Takayama, J. Matsuno, and H. Takagi, *Phys. Rev. B* **83**, 115121 (2011).
- ²⁰K. Tsutsui, T. Tohyama, and S. Maekawa, *Phys. Rev. Lett.* **83**, 3750 (1999).
- ²¹K. Tsutsui, T. Tohyama, and S. Maekawa, *Phys. Rev. Lett.* **91**, 117001 (2003).
- ²²F. H. Vernay, M. J. P. Gingras, and T. P. Devereaux, *Phys. Rev. B* **75**, 020403(R) (2007).
- ²³F. Vernay, B. Moritz, I. S. Elfimov, J. Geck, D. Hawthorn, T. P. Devereaux, and G. A. Sawatzky, *Phys. Rev. B* **77**, 104519 (2008).
- ²⁴T. Nomura and J. Igarashi, *J. Phys. Soc. Jpn.* **73**, 1677 (2004).
- ²⁵T. Nomura and J. Igarashi, *Phys. Rev. B* **71**, 035110 (2005).
- ²⁶T. Nomura and J. Igarashi, *J. Phys. Chem. Solids* **67**, 262 (2006).
- ²⁷J. Igarashi, T. Nomura, and M. Takahashi, *Phys. Rev. B* **74**, 245122 (2006).
- ²⁸M. Takahashi, J. Igarashi, and T. Nomura, *J. Phys. Soc. Jpn.* **77**, 034711 (2008).
- ²⁹R. S. Markiewicz, *Phys. Rev. B* **70**, 174518 (2004).
- ³⁰R. S. Markiewicz and A. Bansil, *Phys. Rev. Lett.* **96**, 107005 (2006).
- ³¹J. van den Brink and M. van Veenendaal, *J. Phys. Chem. Solids* **66**, 2145 (2005).
- ³²J. van den Brink and M. van Veenendaal, *Europhys. Lett.* **73**, 121 (2006).
- ³³L. M. Falicov and J. C. Kimball, *Phys. Rev. Lett.* **22**, 997 (1969).
- ³⁴U. Brandt and C. Mielsch, *Z. Phys. B* **75**, 365 (1989).
- ³⁵J. K. Freericks and V. Zlatić, *Rev. Mod. Phys.* **75**, 1333 (2003).
- ³⁶W. Metzner and D. Vollhardt, *Phys. Rev. Lett.* **62**, 324 (1989).
- ³⁷A. Georges, G. Kotliar, W. Krauth, and M. Rozenberg, *Rev. Mod. Phys.* **68**, 13 (1996).
- ³⁸J. K. Freericks and T. P. Devereaux, *Phys. Rev. B* **64**, 125110 (2001).
- ³⁹J. K. Freericks, T. P. Devereaux, and R. Bulla, *Phys. Rev. B* **64**, 233114 (2001).
- ⁴⁰P. M. Platzman and E. D. Isaacs, *Phys. Rev. B* **57**, 11107 (1998).
- ⁴¹P. Nozierès and E. Abrahams, *Phys. Rev. B* **10**, 3099 (1974).
- ⁴²Nandan Pakhira, J. K. Freericks, and A. M. Shvaika (unpublished).
- ⁴³B. M. McCoy and T. T. Wu, *The Two-Dimensional Ising Model* (Harvard University Press, Cambridge, MA, 1973).
- ⁴⁴A. M. Shvaika and J. K. Freericks, *Condens. Matter Phys.* **11**, 425 (2008).
- ⁴⁵A. M. Shvaika and O. Vorobyov, J. K. Freericks, and T. P. Devereaux, *Phys. Rev. B* **71**, 045120 (2005).
- ⁴⁶A. M. Shvaika, *Condens. Matter Phys.* **9**, 447 (2006).
- ⁴⁷A. M. Shvaika, *Physica C* **341–348**, 177 (2000).
- ⁴⁸J. K. Freericks and P. Miller, *Phys. Rev. B* **62**, 10022 (2000).
- ⁴⁹A. M. Shvaika, *J. Phys. Stud.* **5**, 349 (2001).
- ⁵⁰T. P. Devereaux, G. E. D. McCormack, and J. K. Freericks, *Phys. Rev. B* **68**, 075105 (2003).
- ⁵¹E. Müller-Hartman, *Z. Phys. B* **76**, 211 (1989).
- ⁵²D. Binosi and L. Thußl, *Comput. Phys. Commun.* **161**, 76 (2004).